Article

High-Resolution, Broad-Range Detection Setup for Polarimetric Optical Fiber Sensors

Paweł Wierzba

Department of Metrology and Optoelectronics, Gdansk University of Technology, 80-233 Gdansk, Poland; pwierzba@eti.pg.edu.pl

Featured Application: Polarimetric optical fiber sensors, polarization interferometers.

Abstract: A common-path polarization interferometer using a Wollaston prism and an area detector for the measurement of retardation or optical path difference is presented. Employing a moderate-resolution 1280 by 1024 pixel monochrome camera, it offers a measurement range of approximately 780 radians at 830 nm and 1350 radians at 515 nm while maintaining a high measurement resolution. Retardation introduced by a zero-order waveplate or a Soleil–Babinet compensator was measured to evaluate the performance of the interferometer. Based on the presented measurement results, the resolution of the measurement is estimated to be better than 0.002 rad.

Keywords: polarization; optical fiber sensors; polarization interferometers; Wollaston prism; detection setups

1. Introduction

Polarization interferometers, difference interferometers, and polarimetric optical fiber sensors induce a change in optical path length between orthogonally polarized components of optical radiation in the directions of the principal axes of these devices. In sensors using the Faraday effect, propagating optical radiation undergoes a rotation of the state of polarization. In the case of point sensors, a detection setup converts the information contained in the optical signal into a single value of the measurand. Distributed polarimetric optical fiber sensors must recover information about the value of measurand along the length of sensing fiber.

The selected detection method depends on the principle of operation of a particular sensor and other considerations, such as the measurement range, accuracy, and bandwidth. The reliability, cost, and availability of components are also factors that influence the decision.

In general, distributed polarimetric sensors use detection techniques based on polarization optical time-domain reflectometry (P-OTDR) [1], polarization optical frequency-domain reflectometry (P-OFDR) [2–5], or wavelength-scanning phase-sensitive optical time-domain reflectometry (φOTDR) [6–8].

Point sensors, especially those that employ the Faraday effect, use a polarimeter as their detection setup [9–13] or a polarization division multiplexing detection setup [14]. The detection of signal from difference interferometers is often performed using spectral interferometry with a broadband source and an optical spectrum analyzer (OSA) [15–17] or a tunable laser and a broadband detector [18,19]. The same technique, spectral interferometry, is used in some surface plasmon resonance sensors (SPR) [20–25] and in the characterization of sensitivity to hydrostatic pressure, strain, and temperature of specialty optical fibers [26–28], where it can resolve phase difference as a function of wavelength. Sagnac interferometer detection is also often employed in optical fiber polarimetric sensors [29–31]. Other techniques include tracking interference fringes with photodiodes [32] or the use of diffraction gratings to produce interference fringes that are subsequently detected by a linear detector array [33,34].

Last but not least, polarimetric sensors of hydrostatic pressure, biosensors, and waveguide refractometers often use a detection setup employing a common-path interferometer consisting of a Wollaston prism [34,35] or a birefringent wedge [36–38], followed by a polarizer and a linear detector array (CCD or CMOS). The interferometer produces an equidistant and straight fringe pattern (Young's fringes; fringe interference field) that is recorded by the detector array and processed by a computer, yielding retardation. An accuracy of $2\pi/2100$ rad was demonstrated in [36], with a resolution from $2\pi/4000$ rad [36] to $2\pi/1000$ rad [34]. However, unless continuous tracking of the fringe pattern is performed, the unambiguous measurement range of this method is restricted to 2π rad.

In some instances, retardation must be measured in a range much broader than 2π rad. Such a measurement can be performed by using low coherence interferometry (LCI), i.e., by illuminating the interferometer or sensor with a low-coherence light source and applying a detection technique capable of measuring the optical path difference. In particular, common-path interferometers [34–38] can be used, but the number of fringes on the detector must be increased to allow for tracking of the fringe pattern across the required measurement range. However, as the number of fringes is increased, the number of pixels per fringe is reduced, lowering the resolution and accuracy of the measurement.

The measurement range can be extended without degrading resolution by using a Soleil–Babinet compensator [34] or by introducing a step optical delay line in front of the birefringent wedge or the Wollaston prism and replacing the linear detector array with an area detector array [39]. Such modifications increase the cost and complexity of the detection setup, especially through the use of a custom-made, precision step optical delay line.

In this paper, an alternative method for detecting the optical path difference is presented. Obviating the need for the step optical delay line, it uses a simple common-path interferometer and an area detector array. Phase measurement is performed in a manner similar to the Vernier scale, offering a broad measurement range and a high measurement resolution and making the presented method another application of the Vernier principle in the field of optical fiber sensors [40–42].

2. Materials and Methods

Let us consider the polarization interferometer presented in Figure 1a. A light beam from a single-mode polarization-maintaining (SMPM) fiber is collimated by lens L and impinges on Wollaston prism WP. As the axes of the Wollaston prism are aligned along the axes of the fiber, polarization modes $_oHE_{11}$ and $_eHE_{11}$ do not mix; they deviate from each other after propagating through the prism. They then pass through analyzer A, whose axis forms an angle of 45° with the axes of Wollaston prism WP. Finally, the polarization modes interfere on area image sensor AIS, forming a set of equidistant and straight fringes, as shown in Figure 1b. When one side of the area image sensor AIS is parallel to the direction of fringes, as shown in Figure 1b, the interferometer is equivalent to that described in Ref. [36].
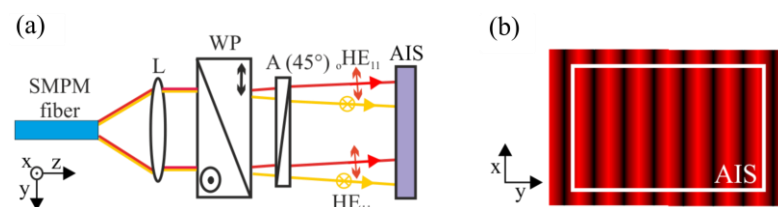

Figure 1. Common-path interferometer for retardation measurement: (**a**) schematic diagram; (**b**) fringe pattern on the detector. L—lens; WP—Wollaston prism; A—analyzer; AIS—area image sensor.

Consider the modification to the interferometer presented in Figure 1 in which the area image sensor AIS is aligned at an angle α to the fringe pattern, as shown in Figure 2. An *xy* coordinate system associated with the image sensor is introduced for the purpose of subsequent analysis.
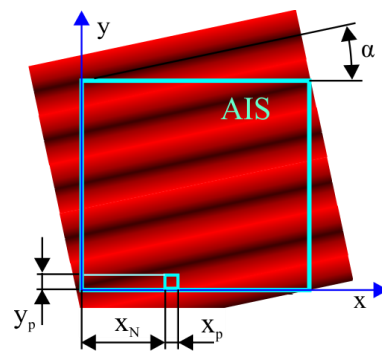
Figure 2. Fringe pattern on the rotated image sensor. AIS—area image sensor.

In order to obtain insight into operation of such a setup without dealing with excessively complicated formulas, let us introduce four simplifying assumptions: (i) the AIS consists of equally spaced pixels of a width x_p and a height y_p; (ii) the AIS is aligned in such a way that the phase difference φ between the two beams interfering at the origin of the coordinate system xy equals the phase difference of interfering beams; (iii) power density p_0 is constant on the area of the detector; and (iv) visibility of the fringe pattern is 1.0. Then, power density of the interference pattern $p(\varphi, x, y)$ can be expressed as:

$$p(\varphi, x, y) = p_0 \left[1 + \cos\left(\varphi + \frac{2\pi}{\Lambda}(x \, \sin\alpha + y \, \cos\alpha) \right) \right], \tag{1}$$

where Λ represents the fringe spacing, α represents the orientation angle, p_0 represents the maximum power density, and φ represents the phase difference of the polarization modes.

The power incident on a pixel from the bottom row of pixels located at a distance x_N from the origin of the xy coordinate system, as shown in Figure 2, can be expressed using (1) as:

$$P(\phi, x_N) = \int_{x_N}^{x_N + x_p} \int_0^{y_p} p_0 \left[1 + \cos\left(\phi + \frac{2\pi}{\Lambda}(x \, \sin\alpha + y \, \cos\alpha) \right) \right] \mathrm{d}y \mathrm{d}x. \tag{2}$$

By setting:

$$\begin{aligned} k_0 &= \frac{2\pi}{\Lambda} \, \sin\alpha, \\ k_1 &= \frac{2\pi}{\Lambda} \, \cos\alpha \end{aligned} \tag{3}$$

using these in (2), we arrive at:

$$P(\varphi, x_N) = p_0 \int_{x_N}^{x_N + x_p} \left(y_p + \frac{1}{k_1} \sin(\varphi + k_0 x + k_1 y_p) - \frac{1}{k_1} \sin(\varphi + k_0 x) \right) \mathrm{d}x. \tag{4}$$

Rewriting (4) as the sum of three integrals and integrating and employing some trigonometric identities, we obtain

$$P(\varphi, x_N) = P_0 + P_1 \cos(\varphi + k_0 x_N + \gamma), \tag{5}$$

where

$$P_0 = p_0 x_p y_p, \tag{6}$$

$$P_1 = \frac{4 p_0}{k_0 k_1} \sin\left(\frac{k_0 x_p}{2} \right) \sin\left(\frac{k_1 y_p}{2} \right), \tag{7}$$

and offset angle γ is given by

$$\gamma = \frac{1}{2}\left(k_0 x_p + k_1 y_p\right), \tag{8}$$

the power P_i incident on the m-th pixel can be expressed using (5) as:

$$P_i(m, \phi) = P(\phi, (m-1)\,x_p) = P_0 + P_1 \cos\left(\phi + (m-1)\,k_0 x_p + \gamma\right), \tag{9}$$

From (9), it can be seen that for a given phase difference φ and the offset angle γ, the power incident on subsequent pixels of the bottom row of the detector array varies as a sampled harmonic function. If angle α is adjusted to fulfill the condition

$$k_0 x_D \geq 2\pi, \tag{10}$$

where x_D is the width of the detector array, at least one period of this harmonic function can be registered.

Let us calculate the phase difference change $\Delta\varphi$ needed to shift the detected pattern P_m by one pixel. This means that

$$P_i(m, \phi) = P_i(m-1, \phi + \Delta\phi), \tag{11}$$

from (9), we have

$$\cos(\varphi + \gamma + k(i-1)x_P) = \cos\left(\varphi + \Delta\varphi + \gamma + k(i-2)x_P\right), \tag{12}$$

which reduces to

$$\Delta\varphi = k_0 x_P. \tag{13}$$

If $k_0 x_D = 2\pi$, and a detector with N pixels in the row is used, Equation (13) becomes

$$\Delta\varphi = \frac{2\pi}{N}. \tag{14}$$

This means that when a detector with 1024 pixels in the row is used, the resolution of phase measurement can be $2\pi/1024$ rad. It may be expected that the resolution can be even better when data proceeding techniques that enable sub-pixel resolution are used.

The resolution of the presented method may degrade when the amplitude P_1 of the harmonic component in Equation (9) is much smaller than P_0, which is similar to working with low-visibility interference fringes.

In order to investigate this issue, let us introduce a parameter V, defined as:

$$V = \frac{\max(P(m, \varphi)) - \min(P(m, \varphi))}{\max(P(m, \varphi)) + \min(P(m, \varphi))}, \tag{15}$$

It should be noted that V is not the visibility of fringes described by Equation (1); it can be regarded as the visibility in a single row of pixels. From Equations (3), (6), (7) and (9), we obtain:

$$V = \frac{P_1}{P_0} = \frac{\sin\left(\frac{2\pi}{\Lambda}\frac{x_p}{2}\sin\alpha\right)}{\frac{2\pi}{\Lambda}\frac{x_p}{2}\sin\alpha}\frac{\sin\left(\frac{2\pi}{\Lambda}\frac{y_p}{2}\cos\alpha\right)}{\frac{2\pi}{\Lambda}\frac{y_p}{2}\cos\alpha}, \tag{16}$$

which is a product of two $\sin(x)/x$ functions. Since the dimensions x_p and y_p of a pixel are much smaller than the fringe spacing Λ, $\sin\alpha$ is much smaller than one and $\cos\alpha \approx 1$, V becomes:

$$V \approx \frac{2\Lambda}{2\pi y_p}\sin\left(\frac{2\pi}{\Lambda}\frac{y_p}{2}\right). \tag{17}$$

For five pixels per fringe, i.e., $\Lambda = 5y_p$, V equals 0.93. This means that the method is capable of operation even when the fringes are closely spaced.

The quantization of the signal in an image sensor is another factor that introduces an error, often referred to as quantization error. In the case of the detection setup presented, this error affects the accuracy of the phase difference measurement.

Most commonly, image sensors use one or more analog-to-digital (A/D) converters that have a resolution ranging from eight to sixteen bits (cf., e.g., [43,44]). In the most prevalent CMOS image sensors, these A/D converters are integrated on the detector chip.

The quantization error is difficult to investigate analytically; therefore, numerical modeling was conducted. First, an analytical description of an ideal image sensor, followed by an ideal N-bit A/D converter, was created. This image sensor is illuminated by the fringe pattern shown in Figure 2. The power incident on each pixel in a row is described by (9). The orientation angle α of the fringe pattern is selected in such a way that the period of the cosine function in (9) is equal to the number of pixels in the row (e.g., 512), i.e., condition (10) becomes $k_0 x_D = 2\pi$. The output is vector $\mathbf{v_c}$, which contains values of power incident on each pixel, corresponding to a given phase difference φ and rounded down to the nearest level of the N-bit A/D converter. The complex fast Fourier transform of vector $\mathbf{v_c}$ produces complex spectrum vector $\mathbf{s_c}$. The phase of the second component of the calculated spectrum $\mathbf{v_c}[1]$ is phase difference φ_F, corresponding to the rounded data (Please note that the first component of $\mathbf{v_c}$, i.e., $\mathbf{v_c}[0]$ is the constant component). The phase error, arising from quantization, is calculated as $\varphi_F - \varphi$. The results of the calculations are presented in Section 3.1.

Testing of the proposed interferometer should focus on its resolution, as the operation of similar interferometers in the fringe counting mode is already well-researched. This requires a means of introducing small amounts of phase difference or optical path length difference into the light incident on the Wollaston prism. A method used in ellipsometry that employs a quarter-wave ($\lambda/4$) plate rotated by angle θ was selected, and a test setup was designed.

A schematic diagram of the test setup is presented in Figure 3. Light from source LS (a laser diode or a superluminescent diode) is collimated by lens L, polarized by a linear polarizer P, and passes through a quarter-wave plate $\lambda/4$. The light then passes through Wollaston prism WP and analyzer A. Finally, the light interferes on the area detector array in camera C, forming the fringe pattern.
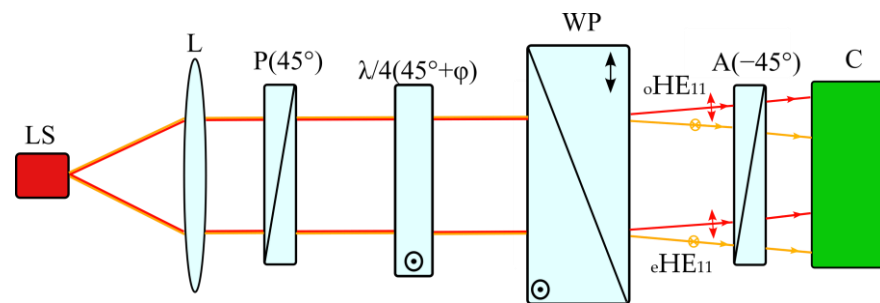

Figure 3. Schematic diagram of the measurement setup. Explanations in the text.

The Jones vector $\mathbf{v_o}$ of light incident on the Wollaston prism can be expressed as:

$$\mathbf{v_o}(\theta) = \mathbf{R}\left(\frac{\pi}{4} + \theta\right) \mathbf{M}_{QWP} \, \mathbf{R}\left(-\frac{\pi}{4} - \theta\right) \mathbf{v}_i, \tag{18}$$

where $\mathbf{R}()$ represents the rotation matrix, θ is the rotation angle of the quarter-wave plate, $\mathbf{M}_{QWP}$ is the matrix of the quarter-wave plate, and $\mathbf{v}_i$ is the Jones vector of the light after the polarizer P. Substituting for $\mathbf{R}$, $\mathbf{M}_{QWP}$, and $\mathbf{v}_i$ in Equation (18) and performing matrix multiplications and some rearrangements, we arrive at:

$$\mathbf{v_o}(\theta) = \frac{1}{\sqrt{2}} \begin{bmatrix} 1 - (1-i)\,(\sin(\theta))^2 - \frac{1}{2}(1-i)\,\sin(2\theta) \\ 1 - (1-i)\,(\sin(\theta))^2 + \frac{1}{2}(1-i)\,\sin(2\theta) \end{bmatrix} = \frac{1}{\sqrt{2}} \begin{bmatrix} m_x \\ m_y \end{bmatrix}. \tag{19}$$

The phase difference $\Delta\varphi$ between the m_x and m_y components of $\mathbf{v_o}$ can be expressed as the argument of (m_x/m_y), viz.:

$$\Delta\varphi(\theta) = \arg\left(\frac{m_x}{m_y}\right) = \arg\left((\cos(2\theta))^2 + i \cdot \sin(2\theta)\right). \tag{20}$$

For small angles (i.e., $|\theta| < 0.105$ rad ($6°$)), $\Delta\varphi$ can be conveniently approximated by

$$\Delta\varphi(\theta) = 2\theta \tag{21}$$

with an approximation error below 2%. If values greater than 0.1 rad of the phase difference $\Delta\varphi$ are needed, a Soleil–Babinet compensator can be used instead of a rotating quarter-wave plate.

A measurement setup was built in the configuration schematically presented in Figure 3. A laser diode or a superluminescent diode was used as the light source LS. The polarizer P and analyzer A were made from a high-contrast polarizing film on a glass substrate. A zero-order quarter-wave plate $\lambda/4$, mounted in a rotation mount (PRM1/M, Thorlabs, Newton, NJ, USA), was used to change the retardation. A Wollaston prism WP made from quartz was used. A monochrome 1280×1024 camera (EO-1312M-GL, Edmund Optics, Mainz, Germany) acquired the fringe pattern, which was sent by a USB link to a PC for image processing.

The quarter-wave plate was rotated by the action of the micrometer actuator in the rotation mount. The rotation of the waveplate was 776 µrad (2.4 arc min) per graduation, corresponding to the retardation change of 1.55 mrad (4.8 arc min), while the full travel of the micrometer head yielded 175 mrad ($10°$) of retardation change.

Additionally, a Soleil–Babinet compensator (i.e., SBC-VIS from Thorlabs or RKQ 10 from B. Halle Nachfl. GmbH, Berlin, Germany) was used in place of the rotated quarter-wave plate. A side view of two configurations of the measurement setup is presented in Figure 4.
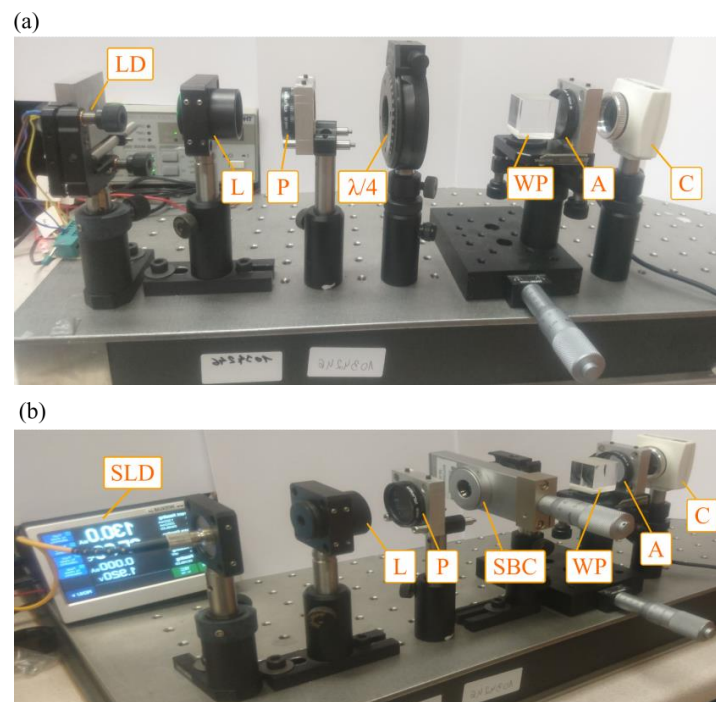

Figure 4. Side view of the measurement setup (**a**) with a laser diode and a quarter-wave plate and (**b**) with superluminescent diode source and a Soleil–Babinet Compensator. LD—laser diode; SLD—superluminescent diode; L—lens; P—polarizer; $\lambda/4$—quarter-wave plate; SBC—Soleil–Babinet Compensator; WP—Wollaston prism; A—analyzer; C—CMOS camera.

3. Results

The influence of the quantization errors on the measurement was investigated first, using a computer model. The results are presented in Section 3.1. The range and resolution of the detection setup were then investigated, as described in Section 3.2.

3.1. Influence of the Quantization Errors

A simple computer model was created in MathCAD (MathCAD v. 15, PTC, Boston, MA, USA), following the description in the previous Section. The model describes an ideal area image sensor with 2^K pixels in a row and an ideal N-bit A/D converter. Parameters K and N were assumed to be positive integers.

Calculations were performed for 256, 512, and 1024 pixels in a row, corresponding to $K = 8$, 9, and 10. For each value of K, the number of bits N in the A/D converter was varied from 8 to 10 to 12. The phase difference φ was changed in the range corresponding to the shift of intensity pattern (9) by one pixel, i.e., $2\pi/2^K$ rad, with an increment equal to 0.001 of the range.

First, the phase error of an ideal area image sensor with 256 pixels in a row and an ideal N-bit A/D converter was calculated using the model. The range of the phase difference φ in that case was 24.5 mrad. Calculation results are presented in Figure 5.
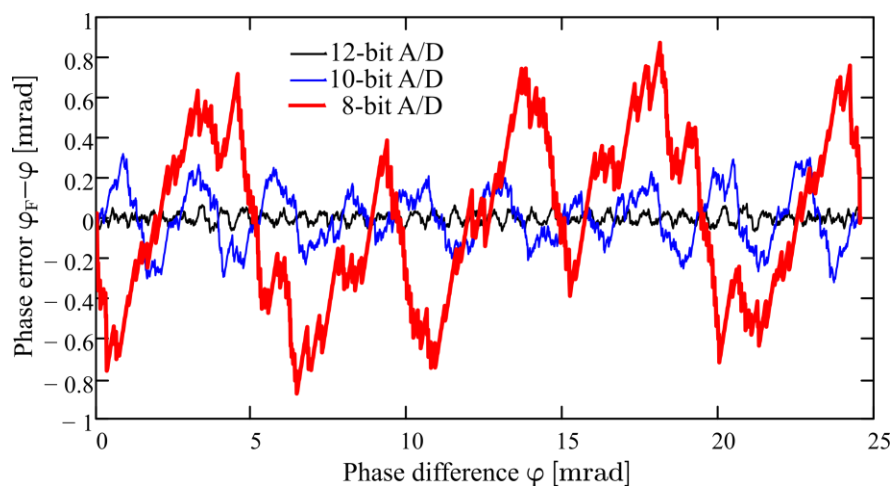

Figure 5. Phase error of image sensor with 256 pixels in a row.

From the data presented in Figure 5, it follows that the magnitude of the error does not exceed 880 μrad for an 8-bit A/D converter, which is $36 \cdot 10^{-3}$ of the range corresponding to one pixel. For a 12-bit A/D converter, the magnitude of error is below 72 μrad, i.e., $2.9 \cdot 10^{-3}$ of the range.

The phase error of an ideal area image sensor with 512 pixels in a row and an ideal N-bit A/D converter was then calculated. The range of phase difference φ in that case was 12.3 mrad. The phase error is shown in Figure 6.

Based on the data presented in Figure 6, it can be concluded that the magnitude of the error does not exceed 474 μrad for an 8-bit A/D converter, which is $39 \cdot 10^{-3}$ of the range corresponding to one pixel. For a 12-bit A/D converter, the magnitude of error is below 55 μrad, i.e., $4.4 \cdot 10^{-3}$ of the range.

Finally, the calculations were repeated for an image sensor with 1024 pixels in a row and an ideal N-bit A/D converter. The range of phase difference φ in that case was 6.14 mrad. The phase error is shown in Figure 7.

The magnitude of the error did not exceed 350 μrad for an 8-bit A/D converter, which is $57 \cdot 10^{-3}$ of the range corresponding to one pixel. For a 12-bit A/D converter, the magnitude of error was below 41 μrad, i.e., $6.7 \cdot 10^{-3}$ of the range.
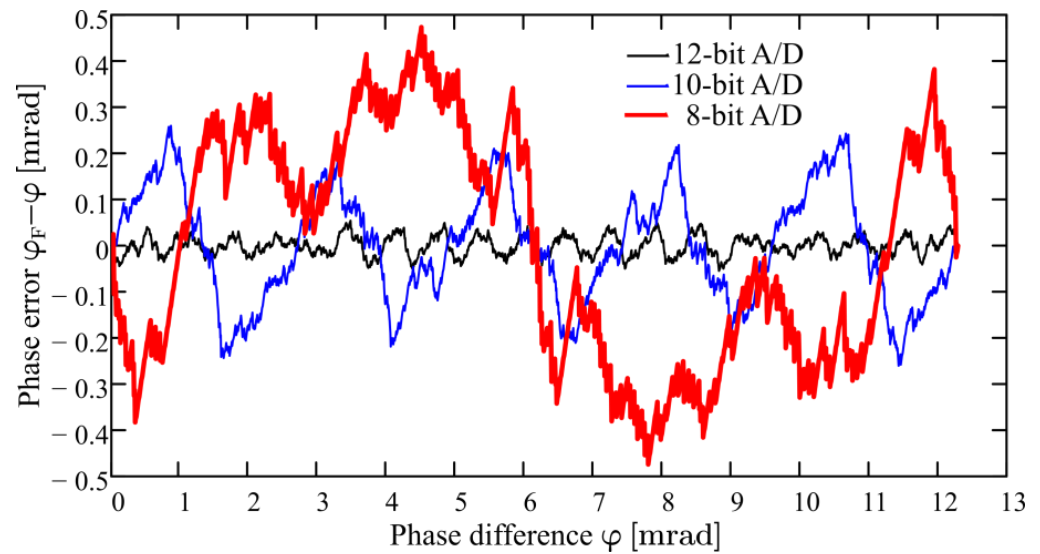
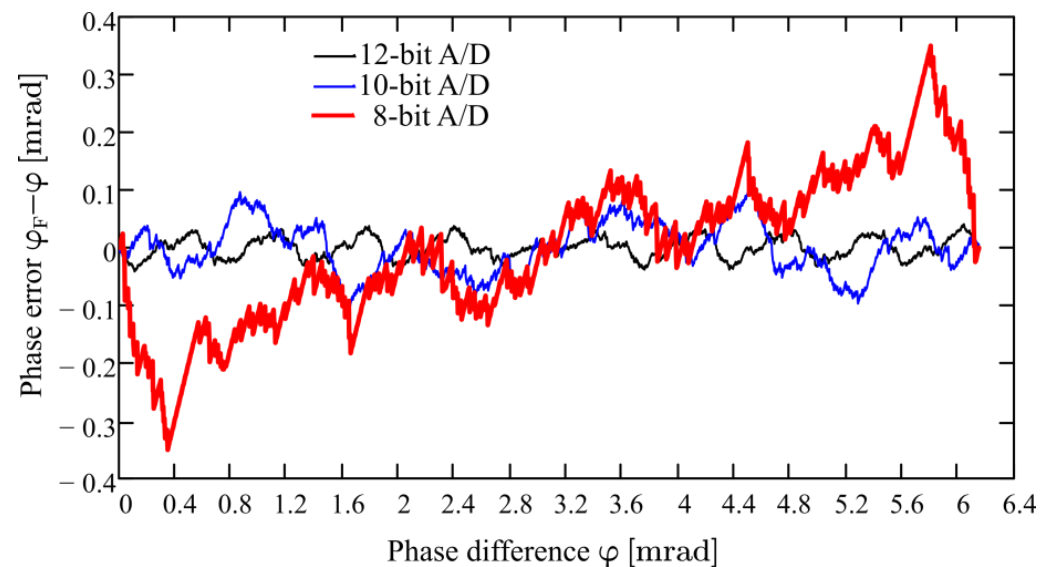**Figure 6.** Phase error of image sensor with 512 pixels in a row.

Figure 7. Phase error of image sensor with 1024 pixels in a row.

While this indicates that the presented detection setup can perform measurements with a sub-pixel resolution, the influence of non-idealities and noise in the image sensor and in the A/D converters may degrade this resolution substantially.

3.2. Range and Resolution

The setup was then carefully aligned, and its operation was tested. First, a laser diode emitting at $\lambda = 515$ nm (PLT5 510, ams-OSRAM International, Premstätten, Austria) was used as the light source. Its operating current was set above the lasing threshold. The fringe pattern incident on the area image sensor was aligned with fringes parallel to the shorter side of the sensor. Part of that pattern is presented in Figure 8a. Subsequently, the laser diode was replaced by a superluminescent diode emitting at $\lambda = 830$ nm (SLD830S-A10W with CLD1015 controller, Thorlabs, Newton, NJ, USA), and the fringe pattern was recorded and is presented in Figure 8b.
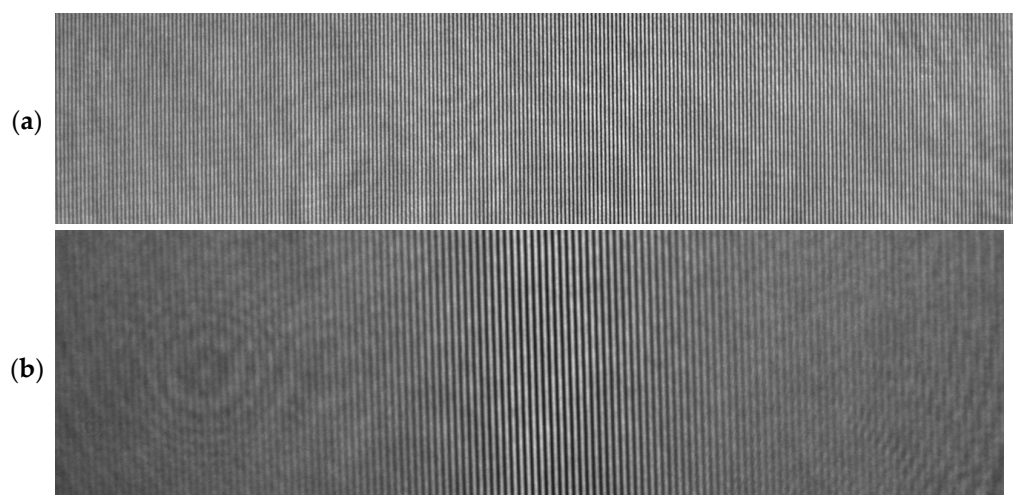
Figure 8. Fringe pattern fragment recorded by the image sensor. (**a**) Illumination with a laser diode emitting at 525 nm; (**b**) illumination with a superluminescent diode emitting at 830 nm.

The fringe pattern in Figure 8a consists of 239 fringes distributed equally on 1280 pixels, i.e., 5.36 pixels per fringe. The contrast is uniform across the pattern, as expected for a laser source. The use of a broadband source to obtain the fringe pattern presented in Figure 8b resulted in a contrast of the fringes that varied across the pattern, being the highest in the central part of pattern and decreasing to zero at the edges of the pattern. In this case, the central part of the fringe pattern (610 pixels) contains 66 fringes, corresponding to 9.24 pixels per fringe and 139 fringes in the entire fringe pattern.

In both fringe patterns from Figure 8, artifacts from dust and imperfections of the optical surfaces are apparent.

A first attempt at measuring retardation was performed with the laser diode emitting at λ = 525 nm and its operating current set below the lasing threshold. The fringe pattern on the camera was aligned to have more than one period of the pattern on one row but not more than two such periods. Unfortunately, small variations in the phases of interfering beams affected the shape of the fringes, resulting in a substantial distortion of the data that were to be analyzed. An example of such a pattern is shown in Figure 9.
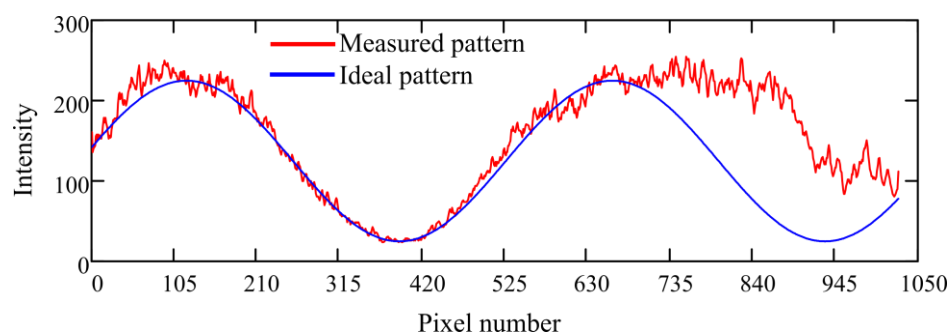

Figure 9. Distorted measured data pattern recorded by one row of pixels and pattern expected from (9).

Most likely, the variations in the phases of the interfering beams arose from the lack of planarity of the interfering beams and the local imperfections of optical components, in particular the lens L, polarizer P, and analyzer A, as these components are usually manufactured with moderate attention to their phase characteristics. Aberrations introduced by these components and the Wollaston prism WP and parasitic effects due to speckles or dust were also responsible for these variations. Unfortunately, the quality of the phase measurement results was rather poor, necessitating a change of approach.

Therefore, a second attempt at measuring the retardation was made with the supler-luminescent diode emitting at λ = 830 nm. The fringe pattern on the camera was aligned to have three to four periods of the pattern on one row. This reduced the resolution but improved the quality of the data.

The fringe pattern was then recorded as a function of retardation. Measurements were performed by changing retardation in one direction to avoid hysteresis and backlash. The position of the fringe pattern was determined by finding the location of a selected minimum. This was accomplished by approximating a fragment of the pattern close to the minimum with a quadratic function and finding the minimum of that function, as illustrated in Figure 10. The position of that minimum, expressed in pixels, was treated as the output signal of the detection setup.
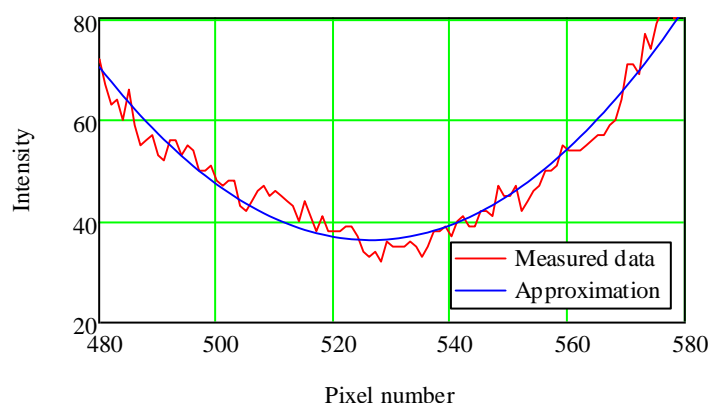

Figure 10. Fragment of measured data pattern recorded by one row of pixels and quadratic function approximating that fragment of the pattern.

The response of the detection setup was plotted against the set retardation, and it is shown in Figure 10.

Based on data shown in Figure 11 and the behavior of the experimental setup, it can be concluded that the resolution of presented setup is approximately 2 mrad (0.11°) or $2\pi/3000$ rad. The conversion factor k_φ, links the response of the setup expressed in the number of pixels ΔN with measured retardation $\Delta\varphi$, i.e.,

$$k_\varphi = \frac{\Delta N}{\Delta\varphi} \tag{22}$$

was determined to be 57.8 pixels/rad, which corresponds to 363 pixels per 2π rad of the measured phase shift.
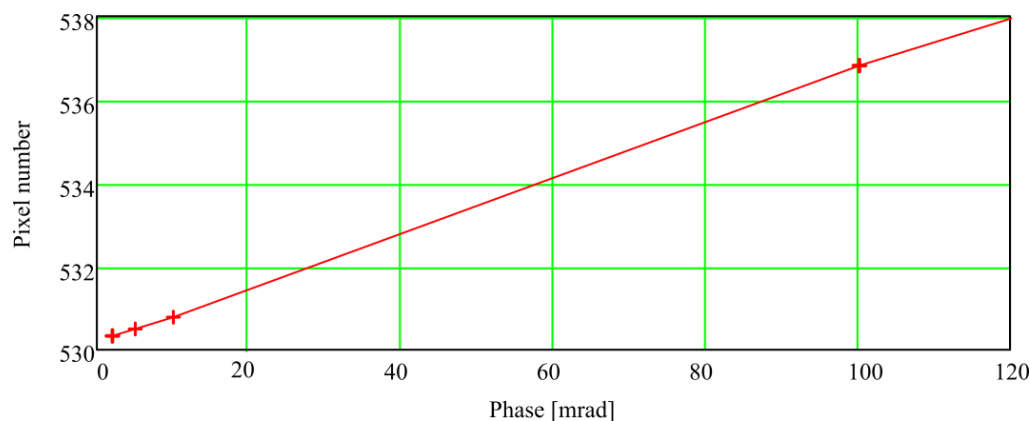

Figure 11. Response of the detection setup to set retardation.

4. Discussion

An analysis of the influence of the quantization errors on the accuracy of the measurement yielded some expected and some unexpected results. As expected, the calculated error decreases with the increasing resolution of the A/D converter. The decrease is not exactly proportional to the increase in the resolution. When moving from an 8-bit resolution to a 10-bit resolution, the error is reduced by less than four times, as one would expect, while moving from a 10-bit resolution to a 12-bit resolution can yield a reduction that is greater or smaller than four times.

While the error decreases with an increasing number of points in the row, interesting behavior is observed for the 8-bit resolution and 512 and 1024 pixels (Figures 5 and 6, respectively), for which the peak-to-peak error decreases by only 24%, while a much greater *average* error reduction is readily apparent. This may be an indication that a more in-depth investigation into the behavior of this error should be performed in the future. At present, however, we should note that predicted error is sufficiently small for the measurement resolutions obtained in this paper.

It should also be noted here that in most available CMOS image sensors, the analog-to-digital conversion is internally performed with a resolution of 10–14 bits (cf. e.g., [43]), and the result is subsequently rounded down to 8–10 bits. Consequently, the eight-bit output exhibits little nonlinearity.

The measurement range of the presented interferometer depends on the number of fringes in the field of view of the detector. However, since the identification of the central fringe in the fringe pattern is often difficult based only on its amplitude, the shape of the interference pattern is often used for that purpose. This requires that some fringes from both sides of the central fringe always be visible, restricting the movement of the central fringe by a margin on both sides of the detector. It can be safely assumed that this margin can be 5% of the total number of fringes, corresponding to twelve and seven fringes for the two cases discussed in the previous Section. Therefore the fringe pattern is allowed to move by 215 fringes or 125 fringes, which corresponds to the measurement range of 1352 rad and 786 rad.

While setups using other detection methods, such as a polarization analysis [9–13], can attain such a range, they are only capable of doing so by tracking the change in the state of polarization, with any interruption of the tracking process invalidating the measurement. Setups employing low-coherence interferometry [34–39] can also attain such a measurement range, but this typically comes at the cost of a reduced measurement resolution.

The demonstrated resolution of the presented interferometer (0.002 rad) is comparable to the resolution of setups using polarization analysis or low-coherence interferometry. Further work is needed to provide a better, more accurate evaluation of this parameter. In particular, a setup for generating retardance with an improved resolution and accuracy must be devised.

Temperature is a factor that limits the performance of the presented interferometer. It can be shown that temperature affects its performance mainly via the change of the birefringence of the material from which the Wollaston prism is made. In the experiments presented in this paper, a prism made from quartz was used. The birefringence Δn of quartz, measured at room temperature (25 $^\circ$C) at a wavelength of 632.8 nm, is approximately $9.02 \cdot 10^{-3}$, while its change with temperature δn is approximately $1.0 \cdot 10^{-6}$ per $^\circ$C (cf. e.g., Figure 4 in [45]).

Using the properties of the Wollaston prism, it can be demonstrated that the measured phase difference $\Delta \varphi$ is proportional (to a good approximation) to the birefringence Δn of the material from which the prism was made, i.e.,

$$\Delta \varphi = k \cdot \Delta n. \tag{23}$$

The measurement error $\delta \varphi$ due to the temperature change is

$$\delta \varphi = k \cdot \delta n. \tag{24}$$

Combining Equations (23) and (24), we obtain

$$\delta\varphi = \frac{\delta n}{\Delta n}\Delta\varphi.$$ (25)

For $\Delta\varphi$ = 1000 rad, the measurement error $\delta\varphi$ is 0.11 rad/°C. This is a large value when compared with the resolution of the presented set-up (0.002 rad). Reducing this error would require either keeping the setup in a constant-temperature environment, or using a method in which the setup is periodically illuminated by a reference beam from a source whose wavelength is independent from temperature, and the arising fringe pattern is used to recalibrate the setup. Alternatively, designs based on an athermalized Mach–Zehnder interferometer or on Fresnel's mirrors can be considered.

The functionality of the discussed interferometer can be implemented using a Mach–Zehnder interferometer, which offers three important advantages in this application. First, when an athermalized design is used, its sensitivity to temperature can be greatly reduced compared to that of the presented interferometer. Second, it can be aligned in such a way that the region of the localization of fringes coincides with the area image detector [46]. Third, the spacing of the interference fringes can be varied by changing the orientation of the mirrors of this interferometer. However, a potential disadvantage of this implementation is the presence of multiple reflective surfaces whose imperfections can introduce distortion into the fringe pattern, degrading accuracy or even preventing the correct operation of such a setup. Moreover, the mechanical stability of such a setup, as well as its susceptibility to vibration, can limit the usability of such a setup. In spite of this, further work will be performed on its implementation.

Finally, the scope of application of the presented interferometer can be extended to sensors in which two beams of the same polarization interfere, such as those described in [47].

5. Conclusions

A common-path polarization interferometer using a Wollaston prism and an area detector for the measurement of retardation or optical path difference was demonstrated. The measurement range of this interferometer is approximately 1350 rad at 515 nm and 786 rad at 830 nm, and it can be altered by using a Wollaston prism with a different splitting angle or a camera with a different pixel size.

The resolution of this interferometer was investigated in a test setup using a Soleil–Babinet compensator or a quarter-wave plate to change the retardation. Based on the experimental results, it can be concluded that the minimum detectable phase change is 0.002 rad. The resolution can be further improved by using a better camera and pre-processing the acquired images more carefully. Using better-quality polarizers and lenses should also result in an improvement in resolution and accuracy.

The presented interferometer offers a measurement resolution comparable with that of the setups described in [36], as well as measurement range of around 1000 rad, which was unattainable for these setups.

Until quite recently, this interferometer was capable of operation only in the spectral range from approximately 400 nm to 1000 nm, limited by the spectral sensitivity characteristics of silicon CCD/CMOS detectors, excluding its use in sensors operating in 1310 nm and 1550 nm bands. At present, the commercial availability of InGaAs image sensors and cameras allows for the presented interferometer to also work in the spectral range from 700 nm to 1700 nm. However, its operation in the mid-infrared range, where sensing fibers are being developed [48,49], will not soon be possible due to the lack of array detectors that are sensitive in that range.

Institutional Review Board Statement: Not applicable.

Informed Consent Statement: Not applicable.

Data Availability Statement: Not applicable.

Conflicts of Interest: The author declares no conflict of interest.

References

1. Wuilpart, M.; Ravet, G.; Megret, P.; Blondel, M. Polarization mode dispersion mapping in optical fibers with a polarization-OTDR. *IEEE Photon. Technol. Lett.* **2002**, *14*, 1716–1718. [CrossRef]
2. Caron, S.; Paré, C.; Paradis, P.; Trudeau, J.-M.; Fougères, A. Distributed fibre optics polarimetric chemical sensor. *Meas. Sci. Technol.* **2006**, *17*, 1075–1081. [CrossRef]
3. Khomenko, A.; Shlyagin, M.; Miridonov, S.; Tentori, D. Wavelength-scanning technique for distributed fiber-optic sensors. *Opt. Lett.* **1998**, *18*, 2065–2067. [CrossRef] [PubMed]
4. Palmieri, L.; Sarchi, D.; Galtarossa, A. Distributed measurement of high electric current by means of polarimetric optical fiber sensor. *Opt. Express* **2015**, *23*, 11073–11079. [CrossRef]
5. Yu, Z.; Zhuang, Q.; Lin, Y.; Lin, Y.; Lin, C.; Rang, B.; Yuan, Y.; Yang, J.; Wen, K.; Xu, P.; et al. Optical frequency domain polarimetry for distributed polarization crosstalk measurement beyond a 110 dB dynamic range. *Opt. Lett.* **2022**, *47*, 4271–4274. [CrossRef]
6. Mikhailov, S.; Matthes, A.; Bierlich, J.; Kobelke, J.; Wondraczek, K.; Berghmans, F.; Geernaert, T. Highly birefringent microstructured optical fiber for distributed hydrostatic pressure sensing with sub-bar resolution. *Opt. Express* **2022**, *30*, 19961–19973. [CrossRef] [PubMed]
7. Zhang, L.; Yang, Z.; Szostkiewicz, Ł.; Markiewicz, K.; Mikhailov, S.; Geernaert, T.; Rochat, E.; Thévenaz, L. Long-distance distributed pressure sensing based on frequency-scanned phase-sensitive optical time-domain reflectometry. *Opt. Express* **2021**, *29*, 20487–20497. [CrossRef] [PubMed]
8. Mikhailov, S.; Zhang, L.; Geernaert, T.; Berghmans, F.; Thevenaz, L. Distributed Hydrostatic Pressure Measurement Using Phase-OTDR in a Highly Birefringent Photonic Crystal Fiber. *J. Light. Technol.* **2019**, *37*, 4496–4500. [CrossRef]
9. Ramakrishnan, M.; Rajan, G.; Semenova, Y.; Lesiak, P.; Domański, A.; Woliński, T.; Boczkowska, A.; Farrell, G. The influence of thermal expansion of a composite material on embedded polarimetric sensors. *Smart Mater. Struct.* **2011**, *20*, 125002. [CrossRef]
10. Nikoniuk, D.; Bednarska, K.; Sienkiewicz, M.; Krzesiński, G.; Olszyna, M.; Dähne, L.; Woliński, T.R.; Lesiak, P. Polymer Fibers Covered by Soft Multilayered Films for Sensing Applications in Composite Materials. *Sensors* **2019**, *19*, 4052. [CrossRef]
11. Torbus, S.A.; Michalski, J.A. Testing of a Polarimetric Current Sensor in the Frequency Domain. *Sensors* **2021**, *21*, 3008. [CrossRef]
12. Nasilowski, T.; Skorupski, K.; Makara, M.; Statkiewicz-Barabach, G.; Mergo, P.; Marc, P.; Jaroszewicz, L. Very high polarimetric sensitivity to strain of second order mode of highly birefringent microstructured fibre. *Proc. SPIE* **2011**, *7753*, 77533O-1–77533O-4.
13. Tenderenda, T.; Skorupski, K.; Makara, M.; Statkiewicz-Barabach, G.; Mergo, P.; Marc, P.; Jaroszewicz, L.R.; Nasilowski, T. Highly birefringent dual-mode microstructured fiber with enhanced polarimetric strain sensitivity of the second order mode. *Opt. Express* **2012**, *20*, 26996–27002. [CrossRef] [PubMed]
14. Xu, S.; Li, W.; Xing, F.; Wang, Y. Polarimetric current sensor based on polarization division multiplexing detection. *Opt. Express* **2014**, *22*, 11985–11994. [CrossRef] [PubMed]
15. Okda, H.A.; Rabia, S.I.; Shalaby, H.M.H. Sensitivity enhancement of a difference interferometer refractive index sensor based on a silicon-on-insulator hybrid plasmonic waveguide. *JOSA* **2021**, *38*, 1405–1415. [CrossRef]
16. Liu, Q.; Kim, K.W.; Gu, Z.; Kee, J.S.; Park, M.K. Single-channel Mach-Zehnder interferometric biochemical sensor based on two lateral-mode spiral waveguide. *Opt. Express* **2014**, *22*, 27910–27920. [CrossRef]
17. Debackere, P.; Scheerlinck, S.; Bienstman, P.; Baets, R. Surface plasmon interferometer in silicon-on-insulator: Novel concept for an integrated biosensor. *Opt. Express* **2006**, *14*, 7063–7072. [CrossRef]
18. Liang, Y.; Zhao, M.; Wu, Z.; Morthier, G. Bimodal waveguide interferometer RI sensor fabricated on low-cost polymer platform. *IEEE Photon. J.* **2019**, *11*, 6801108. [CrossRef]
19. Irfan, M.; Khan, Y.; Rehman, A.U.; Butt, M.A.; Khonina, S.N.; Kazanskiy, N.L. Plasmonic Refractive Index and Temperature Sensor Based on Graphene and LiNbO3. *Sensors* **2022**, *22*, 7790. [CrossRef]
20. Gasiora, K.; Martynkien, T.; Mergo, P.; Urbanczyk, W. Fiber-optic surface plasmon resonance sensor based on spectral phase shift interferometric measurements. *Sens. Actuators Chem.* **2018**, *257*, 602–608. [CrossRef]
21. Hlubina, P.; Duliakova, M.; Kadulova, M.; Ciprian, D. Spectral interferometry-based surface plasmon resonance sensor. *Opt. Commun.* **2015**, *354*, 240–245. [CrossRef]
22. Hlubina, P.; Ciprian, D. Spectral phase shift of surface plasmon resonance in the Kretschmann configuration: Theory and experiment. *Plasmonics* **2016**, *12*, 1071–1078. [CrossRef]
23. Rifat, A.A.; Ahmed, R.; Yetisen, A.K.; Butt, H.; Sabouri, A.; Mahdiraji, G.A.; Yun, S.H.; Adikan, F.M. Photonic crystal fiber based plasmonic sensors. *Sens. Actuators Chem.* **2017**, *243*, 311–325. [CrossRef]
24. Wang, D.; Yi, Z.; Ma, G.; Dai, B.; Yang, J.; Zhang, J.; Yu, Y.; Liu, C.; Wu, X.; Bian, Q. Two-channel photonic crystal fiber based on surface plasmon resonance for magnetic field and temperature dual-parameter sensing. *Phys. Chem. Chem. Phys.* **2022**, *24*, 21233–21241. [CrossRef]
25. Zhu, W.; Yi, Y.; Yi, Z.; Bian, L.; Yang, H.; Zhang, J.; Yu, Y.; Liu, C.; Li, G.; Wu, X. High confidence plasmonic sensor based on photonic crystal fibers with a U-shaped detection channel. *Phys. Chem. Chem. Phys.* **2023**, *25*, 8583–8591. [CrossRef]

26. Nielsen, M.D.; Mortensen, N.A. Photonic crystal fiber design based on the V–parameter. *Opt. Express* **2003**, *11*, 2762–2768. [CrossRef]

27. Hlubina, P.; Ciprian, D. Spectral-domain measurement of phase modal birefringence in polarization-maintaining fiber. *Opt. Express* **2007**, *15*, 17019–17024. [CrossRef]

28. Szczurowski, M.K.; Martynkien, T.; Statkiewicz-Barabach, G.; Urbanczyk, W.; Webb, D.J. Measurements of polarimetric sensitivity to hydrostatic pressure, strain and temperature in birefringent dual-core microstructured polymer fiber. *Opt. Express* **2010**, *18*, 12076–12087. [CrossRef]

29. Anuszkiewicz, A.; Martynkien, T.; Olszewski, J.; Mergo, P.; Urbańczyk, W. Polarimetric sensitivity to hydrostatic pressure and temperature in a side-hole fiber with squeezed microstructure. *J. Opt.* **2015**, *17*, 125609. [CrossRef]

30. De, M.; Gangopadhyay, T.K.; Singh, V.K. Prospects of Photonic Crystal Fiber as Physical Sensor: An Overview. *Sensors* **2019**, *19*, 464. [CrossRef]

31. Liu, Z.; Htein, L.; Lee, K.-K.; Lau, K.-T.; Tam, H.-Y. Large dynamic range pressure sensor based on two semicircle-holes microstructured fiber. *Sci. Rep.* **2018**, *8*, 65. [CrossRef] [PubMed]

32. Zinoviev, K.E.; González-Guerrero, A.B.; Domínguez, C.; Lechuga, L.M. Integrated bimodal waveguide interferometric biosensor for label-free analysis. *J. Light. Technol.* **2011**, *29*, 1926–1930. [CrossRef]

33. Zhou, C.; Hedayati, M.K.; Kristensen, A. Multifunctional waveguide interferometer sensor: Simultaneous detection of refraction and absorption with size-exclusion function. *Opt. Express* **2018**, *26*, 24372–24383. [CrossRef] [PubMed]

34. Lukosz, W.; Stamm, C.; Moser, H.; Ryf, R.; Dübendorfer, J. Difference interferometer with new phase-measurement method as integrated-optical refractometer, humidity sensor and biosensor. *Sens. Act.* **1997**, *39*, 316–323. [CrossRef]

35. Martynkien, T.; Statkiewicz-Barabach, G.; Olszewski, J.; Wojcik, J.; Mergo, P.; Geernaert, T.; Sonnenfeld, C.; Anuszkiewicz, A.; Szczurowski, M.K.; Tarnowski, K.; et al. Highly birefringent microstructured fibers with enhanced sensitivity to hydrostatic pressure. *Opt. Express* **2010**, *18*, 15113–15121. [CrossRef]

36. Nakadate, S. High precision retardation measurement using phase detection of Young's fringes. *Appl. Opt.* **1990**, *29*, 242–246. [CrossRef]

37. Nakadate, S. Phase Detection of Equidistant Fringes for Highly Sensitive Optical Sensing. I. Principle and Error Analyses. *J. Opt. Soc. Am.* **1988**, *5*, 1258–1264. [CrossRef]

38. Nakadate, S. Phase Detection of Equidistant Fringes for Highly Sensitive Optical Sensing. II. Experiments. *J. Opt. Soc. Am.* **1988**, *5*, 1265–1269. [CrossRef]

39. Bock, W.J.; Urbanczyk, W. Coherence Multiplexing of Fiber-Optic Pressure and Temperature Sensors Based on Highly Birefringent Fibers. *IEEE Trans. Instrum. Meas.* **2000**, *49*, 392–397. [CrossRef]

40. Lin, W.; Liu, Y.; Liu, Y.; Shum, P.P.; Vai, M.I. Fiber Temperature Sensor Based on Vernier Effect and Optical Time Stretching Method. *Micromachines* **2022**, *13*, 2215. [CrossRef]

41. Mumtaz, F.; Roman, M.; Zhang, B.; Abbas, L.G.; Ashraf, M.A.; Dai, Y.; Huang, J. Highly Sensitive Strain Sensor by Utilizing a Tunable Air Reflector and the Vernier Effect. *Sensors* **2022**, *22*, 7557. [CrossRef] [PubMed]

42. Chen, Y.; Zhao, L.; Hao, S.; Tang, J. Advanced Fiber Sensors Based on the Vernier Effect. *Sensors* **2022**, *22*, 2694. [CrossRef]

43. Onsemi Datasheet, PYTHON 1.3/0.5/0.3 MegaPixels Global Shutter CMOS Image Sensors—NOIP1SN1300A, August 2021−Rev. 6. Available online: https://www.onsemi.com/download/data-sheet/pdf/noip1sn1300a-d.pdf (accessed on 11 April 2023).

44. *Sony Product Information, IMX461AQR Diagonal 55 mm (Type 3.4) CMOS Image Sensor with Square Pixel for Color Cameras, ver 1.0*; Sony Semiconductor Solutions Corporation: Kanagawa, Japan, 2018.

45. Hernández-Rodríguez, C.; Gómez-Garrido, P. Optical anisotropy of quartz in the presence of temperature-dependent multiple reflections using a high-accuracy universal polarimeter. *J. Phys. Appl. Phys.* **2000**, *33*, 2985. [CrossRef]

46. Born, M.; Wolf, E. *Principles of Optics*, 7th ed.; Cambridge University Press: Cambridge, UK, 1999; pp. 348–352.

47. Statkiewicz-Barabach, G.; Olszewski, J.; Mergo, P.; Urbanczyk, W. Hydrostatic Pressure and Temperature Measurements Using an In-Line Mach-Zehnder Interferometer Based on a Two-Mode Highly Birefringent Microstructured Fiber. *Sensors* **2017**, *17*, 1648. [CrossRef] [PubMed]

48. Chen, N.; Chang, M.; Lu, X.; Zhou, J.; Zhang, X. Numerical Analysis of Mid-infrared D-Shaped Photonic-Crystal-Fiber Sensor Based on Surface-Plasmon-Resonance Effect for Environmental Monitoring. *Appl. Sci.* **2020**, *10*, 3897. [CrossRef]

49. Du, Z.; Liu, H. Mid-infrared refractive index photonic crystal fiber sensor based on surface plasmon resonance for ultra-high sensitivity. *Laser Phys.* **2023**, *33*, 016201. [CrossRef]